Editors' Suggestion

Orbital Fulde-Ferrell Pairing State in Moiré Ising Superconductors

Ying-Ming Xie* and K. T. Law†
Department of Physics, Hong Kong University of Science and Technology, Clear Water Bay, Hong Kong, China

(Received 27 January 2023; accepted 9 June 2023; published 5 July 2023)

In this Letter, we study superconducting moiré homobilayer transition metal dichalcogenides where the Ising spin-orbit coupling (SOC) is much larger than the moiré bandwidth. We call such noncentrosymmetric superconductors, moiré Ising superconductors. Because of the large Ising SOC, the depairing effect caused by the Zeeman field is negligible and the in-plane upper critical field (B_{c2}) is determined by the orbital effects. This allows us to study the effect of large orbital fields. Interestingly, when the applied in-plane field is larger than the conventional orbital B_{c2}, a finite-momentum pairing phase would appear which we call the orbital Fulde-Ferrell (FF) state. In this state, the Cooper pairs acquire a net momentum of $2q_B$, where $2q_B = eBd$ is the momentum shift caused by the magnetic field B and d denotes the layer separation. This orbital field-driven FF state is different from the conventional FF state driven by Zeeman effects in Rashba superconductors. Remarkably, we predict that the FF pairing would result in a giant superconducting diode effect under electric gating when layer asymmetry is induced. An upturn of the B_{c2} as the temperature is lowered, coupled with the giant superconducting diode effect, would allow the detection of the orbital FF state.

DOI: 10.1103/PhysRevLett.131.016001

Introduction.—Since the discovery of correlated insulating states and unconventional superconductivity in twisted bilayer graphene [1,2], moiré superlattices have become important platforms for studying correlated physics, superconductivity, and topological states [3]. Recently, these studies have been extended to a new type of moiré materials based on transition metal dichalcogenides (TMD) [4–23]. Notably, the WSe_2 moiré superlattice further shows a possible signature of superconductivity, in which the resistance drops to zero at a critical temperature of about 1 to 3 K [6,16]. Importantly, superconductivity appears when the Fermi energy is near the valence band top of WSe_2 such that the Ising spin-orbit coupling (SOC) is exceedingly large (in the order of hundreds of meV [24]). The Ising SOC, which pins electron spins at opposite momentum to opposite (out-of-plane) directions [25–27], strongly suppresses the effect of in-plane Zeeman field and enhances in-plane upper critical field B_{c2} [26–41]. Because of the large Ising SOC, the Zeeman depairing effect of the magnetic field can be ignored and the superconductivity of the moiré bilayer can only be suppressed by the orbital effects.

In this Letter, we study the role of Ising SOC in superconducting TMDs with moiré bands. Specifically, we show that in-plane B_{c2} of the superconducting states goes beyond the Pauli limit [42,43] but the in-plane B_{c2} is limited by the orbital effect instead of the Zeeman effect. Moreover, we show that the moiré Ising superconductor can be driven to a finite-momentum pairing state at low temperatures by the orbital effects of the magnetic field. Using realistic parameters of twisted bilayer TMDs, we find that the nature of this finite-momentum tends to be a $2q_B$-Fulde-Ferrell (FF) pairing state [44], in which Cooper pairs at both layers carry a finite-momentum around $2q_B$ perpendicular to applied fields. The phase transition from the conventional pairing to the finite-momentum pairing can be detected by the temperature dependence of the upper critical field. Interestingly, we predict a giant superconducting diode effect induced by the $2q_B$-FF pairing under electric gating. The combination of B_{c2} and the diode effect would provide strong evidence of the novel orbital FF state.

Model.—To study the properties of moiré Ising superconductors, we start with a continuum model of twisted homobilayer TMD with Ising SOC and external magnetic fields [5]. We focus on homobilayer TMDs with AA stacking. The lattice constant of each monolayer is denoted by a_0. The top layer and the bottom layer are rotated by an angle of $\theta/2$ and $-\theta/2$, respectively, with respect to one of the transition metal sites [see Fig. 1(a)]. The crystal point group symmetry is D_3, which is generated by a twofold

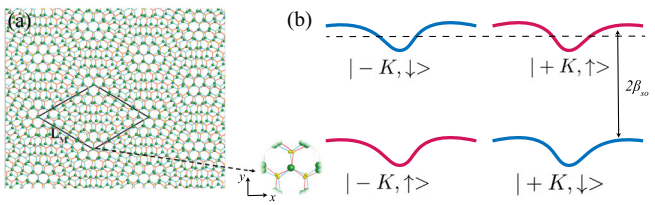

FIG. 1. (a) The lattice structure of a twisted homobilayer TMD. The moiré unit cell is highlighted with L_M as the moiré lattice constant. (b) A schematic plot of the top moiré band of spin-up state and spin-down state at two valleys. Here, $2\beta_{so}$ labels the spin-splitting induced by the Ising SOC.

rotation C_{2y} along the y axis and a threefold rotation C_{3z} along the z axis. It is important to note that inversion symmetry is broken in the moiré bilayer TMD such that the superconducting state can be different from the centrosymmetric bilayer TMD studied in Ref. [45].

The moirè superlattice, which has a moirè lattice constant of $L_M = a_0/\sin\theta$, folds the energy bands and gives rise to the moirè Brillouin. The moirè bands under a finite in-plane magnetic field are described by the Hamiltonian

$$H_\xi(\boldsymbol{r}) = \begin{pmatrix} h_b(\boldsymbol{r}) & \hat{T}(\boldsymbol{r}) \\ \hat{T}^\dagger(\boldsymbol{r}) & h_t(\boldsymbol{r}) \end{pmatrix}, \tag{1}$$

where $\xi = \pm$ is the valley index for $\pm\boldsymbol{K}$ valley. Here the Hamiltonian of each individual layer is given by

$$\begin{aligned} h_l(\boldsymbol{r}) = &-\frac{1}{2m^*}(\hat{\boldsymbol{p}} + \boldsymbol{q_B}\tau_z - \xi\boldsymbol{K}_l)^2 - \mu + \Omega_\xi^{(l)}(\boldsymbol{r}) \\ &- \xi\beta_{so}s_z + u_B\boldsymbol{B}\cdot\boldsymbol{s}, \end{aligned} \tag{2}$$

where $l = t(b)$ labels the top (bottom) layer, m^* denotes the effective mass of valence band, μ is the chemical potential, and τ_i and s_i are Pauli matrices defined in layer and spin space, respectively. The β_{so} characterizes the strength of Ising SOC. The orbital effect of an external magnetic field introduces a momentum shift $q_B = |\boldsymbol{q_B}| = eBd/2$ with $\boldsymbol{q_B} = e\boldsymbol{A}$ and $\boldsymbol{A} = \frac{1}{2}d\boldsymbol{B}\times\hat{\boldsymbol{z}}$ as the chosen gauge potential, where $\boldsymbol{B}$ denotes the in-plane external magnetic field, d denotes the interlayer distance, e is the electron charge. The Zeeman effect of the external magnetic field is captured by the last term, where the g factor is taken to be 2 and u_B denotes the Bohr magneton. $\Omega_\xi^{(l)}(\boldsymbol{r})$ is the intralayer moiré potential, and $\hat{T}(\boldsymbol{r})$ is the interlayer moiré potential. The detailed form of moiré potentials and the model parameters adopted from Ref. [9] are presented in Supplemental Material, Sec. I [46].

We describe the superconducting twisted homobilayer TMD by a mean-field Hamiltonian, which is written as

$$H_{MF}(\boldsymbol{r}) = H(\boldsymbol{r}) + \sum_\xi \Psi_\xi^\dagger(\boldsymbol{r})\hat{\Delta}(\boldsymbol{r})\Psi_{-\xi}^\dagger(\boldsymbol{r}) + \text{H.c.} \tag{3}$$

Here the moiré Hamiltonian is

$$H(\boldsymbol{r}) = \sum_\xi \int d\boldsymbol{r}\Psi_\xi^\dagger(\boldsymbol{r})\mathcal{H}_\xi(\boldsymbol{r})\Psi_\xi(\boldsymbol{r}) \tag{4}$$

and $\Psi_\xi(\boldsymbol{r}) = (\psi_{\xi b\uparrow}, \psi_{\xi b\downarrow}, \psi_{\xi t\uparrow}, \psi_{\xi t\downarrow})^T$ denotes a four-component electron annihilation operator. The pairing matrix $\hat{\Delta}(\boldsymbol{r})$ is represented in the layer and spin space. Because of the layered structure, we expect the pairings to be within electrons of the same layer that can be classified with irreducible representations of the D_3 point group (see Supplemental Material, Sec. I [46]). The favored pairing form is determined by the microscopic interaction. In this work, for illustrative purposes, we consider the two conventional gapped intralayer pairings: $\hat{\Delta}_{A_1} = \Delta i s_y$ and $\hat{\Delta}_{A_2} = \Delta i\tau_z s_y$, where A_1, A_2 label the irreducible representations of D_3. Here, we consider both A_1 and A_2 pairings as they would generally be mixed by in-plane magnetic fields in the case of finite-momentum pairings.

The enhanced in-plane upper critical field B_{c2}.—The in-plane B_{c2} of the moiŕe Ising superconductor can be obtained from the linearized gap equation

$$U_0\chi_s(\boldsymbol{q}, \boldsymbol{B}, T) = 1. \tag{5}$$

Here, U_0 denotes the interaction strength that stabilizes the $A_{1(2)}$ pairing, $\boldsymbol{q}$ is to take account of the possible finite pairing momentum, T is the temperature and the superconducting susceptibility $\chi_s(\boldsymbol{q}, \boldsymbol{B}, T)$, in general, is given by the maximal eigenvalue of the pairing susceptibility matrix

$$\hat{\chi}(\boldsymbol{q}, \boldsymbol{B}, T) = \begin{pmatrix} \chi_{11}(\boldsymbol{q}, \boldsymbol{B}, T) & \chi_{12}(\boldsymbol{q}, \boldsymbol{B}, T) \\ \chi_{21}(\boldsymbol{q}, \boldsymbol{B}, T) & \chi_{22}(\boldsymbol{q}, \boldsymbol{B}, T) \end{pmatrix}. \tag{6}$$

The susceptibility matrix is expressed in the $\hat{\Delta}(\boldsymbol{q}) = (\Delta_{A_1}(\boldsymbol{q}), \Delta_{A_2}(\boldsymbol{q}))^T$ space. More details of the calculations for the pairing susceptibility and the B_{c2} from the Hamiltonian $H_0(\boldsymbol{p}, \boldsymbol{B})$ can be found in the Supplemental Material, Sec. VI [46]. To be specific, we would fix the filling at $\nu \approx -0.6$ in our calculations and set the field direction along the x direction. In general, a threefold anisotropy would be expected for the upper critical field. In the main text, we set the twist angle $\theta = 5°$, near where the possible signature of superconductivity would appear in the experiment [6].

The calculated in-plane B_{c2} of the zero-momentum pairing with $\boldsymbol{q} = 0$ is shown in Fig. 2. Figure 2(a) displays the corresponding moiré energy bands at K valley, where the spin of the top moiré band that contributes to the

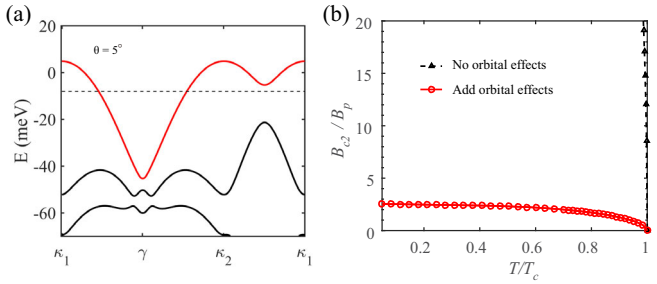

FIG. 2. (a) The moiré bands of a homobilayer TMD with twist angle $\theta = 5°$, where the top moiré bands are highlighted in red. (b) The in-plane upper critical field B_{c2} (in units of Pauli limit $B_p \approx 1.86T_c$) as a function of temperature (in units of the zero-field critical temperature) with (in red) and without (in blue) orbital effects of the magnetic field. We set $T_c = 1$ K and fix the chemical potential at $\nu \approx -0.6$ [the black dashed line in (a)] in (b).

superconductivity (in red) is fully polarized by the Ising SOC. In this case, the in-plane critical magnetic field B_{c2} (in the unit of the Pauli limit B_p) versus critical temperature T (in units of zero-field critical temperature T_c) curves are plotted in Fig. 2(b), where the orbital effects are present or absent according to Eq. (2). When the orbital effects are artificially turned off while the Zeeman effects are included, it can be seen that the superconducting critical temperature is almost insensitive to the external fields due to the strong Ising SOC. In contrast, the in-plane B_{c2} would ultimately be limited to several B_p when orbital effects are included (red line). This stands in sharp contrast to superconducting MoS_2 and $NbSe_2$ where the depairing due to the paramagnetic effect is dominant because of the much smaller Ising SOC at the Fermi energy in these materials.

To estimate the magnitude of the resulting orbital effect limited B_{c2}, we can construct a phenomenological GL free energy theory by taking the order parameter of top and bottom layer to be $\Delta_t \equiv |\Delta| e^{i\varphi_t}$ and $\Delta_b \equiv |\Delta| e^{i\varphi_b}$, respectively. The Ginzburg-Landau (GL) free energy that captures our system can be written as (see Supplemental Material, Sec. V for more details [46])

$$\mathcal{F}(|\Delta|) = -(\alpha_0 - \alpha_1(B))|\Delta|^2 + \frac{\beta_0}{2}|\Delta|^4 + \lambda_J(1 - \cos(\varphi_t - \varphi_b))|\Delta|^2. \quad (7)$$

Here, $\alpha_0 \propto (T_c - T)$ and β_0 are the GL coefficients, $\alpha_1(B)$ to the second order can be approximated as $\alpha_1(B) = \Lambda q_B^2$. Λ depends on the electron effective mass and interlayer coupling. λ_J denotes the Josephson coupling strength between two layers. As expected, the critical field B_{c2} for zero-momentum pairing is determined by the A_1 pairing, where $\varphi_t = \varphi_b$ to minimize the Josephson coupling energy. According to the coefficient of $|\Delta|^2$, the upper critical field is now estimated as

$$B_c = \sqrt{\frac{4\alpha_0}{e^2 d^2 \Lambda}}. \quad (8)$$

Therefore, the orbital effect limited $B_{c2} \propto \sqrt{T_c - T}$ is mainly determined by the effective mass and thickness. Note that the effective mass strongly depends on the twist angle. As shown in Supplemental Material, Sec. III [46], the in-plane B_{c2} can be enhanced prominently when we artificially decrease the twist angle.

Orbital Fulde-Ferrell pairing state.—Next, we study the case of finite-momentum pairings with $\boldsymbol{q} \neq 0$ induced by the orbital effects of magnetic fields. The stabilized finite-momentum pairing is expected to be $\boldsymbol{q} = (0, q)$, as the orbital motion of electrons is perpendicular to the in-plane magnetic fields. To find the robust q driven by the in-plane magnetic fields, we display the critical field B_c as a function of q in Fig. 3(a) at various temperatures with $T = (0.9, 0.5, 0.1)T_c$. Here, we have used the magnitude of the momentum shift $q_B = |\boldsymbol{q_B}|$ as defined in Eq. (2) as a natural unit for the pairing momentum q. The robust finite-momentum pairing can be determined by the one with q that maximizes the critical field B_{c2}. Notably, although the zero-momentum pairing $q = 0$ is favored near the critical temperature, a prominent $q \approx \pm 2q_B$ pairing becomes favorable at low temperatures. Figure 3(b) displays the superconducting pairing χ_s versus B curve at $q = 0$ and $|q| = 2q_B$. It clearly shows that the finite-momentum pairing state with $|q| = 2q_B$ exhibits a higher B_{c2} than the zero-momentum pairing state. This $2q_B$ finite-momentum pairing can be understood from the momentum shift induced by orbital effects. The momentum of electrons at two opposite valleys, which would pair together, obtains the same q_B momentum shift according to Eq. (2).

To understand the nature of this $2q_B$-finite-momentum pairing, we can check the finite-momentum pairing susceptibility $\chi_{ij}(q = 2q_B)$ versus B. The stabilized pairing form could be obtained from the pairing susceptibility matrix Eq. (6), which can be written as

$$\Delta(\boldsymbol{r}) = \sum_{\boldsymbol{q}} \Delta_{\boldsymbol{q}} \left(\cos\frac{\theta_{\boldsymbol{q}}}{2} + \sin\frac{\theta_{\boldsymbol{q}}}{2}\tau_z \right) i\sigma_y e^{i\boldsymbol{q}\cdot\boldsymbol{r}}. \quad (9)$$

Here, $[\cos(\theta_{\boldsymbol{q}}/2), \sin(\theta_{\boldsymbol{q}}/2)]^T$ represents the corresponding eigenvector of χ_s with $\theta_{\boldsymbol{q}} = \arcsin(\chi_{12}/\sqrt{(\chi_{11} - \chi_{22})^2/4 + \chi_{12}^2})$. Because of the presence of finite interlayer coupling, the resulting finite-momentum pairing susceptibility $\chi_{11} - \chi_{22} \gg \chi_{12}$ so that $\theta_{\boldsymbol{q}} \approx 0$ (Supplemental Material, Sec. III [46]). As a result, according to Eq. (9), the stabilized pairing form behaves as a FF pairing, which can be parametrized as $\Delta(\boldsymbol{r}) = |\Delta| e^{i\boldsymbol{q}\cdot\boldsymbol{r}}$ or $\Delta(\boldsymbol{r}) = |\Delta| e^{-i\boldsymbol{q}\cdot\boldsymbol{r}}$ with $q = (0, 2q_B)$ (see an illustration in the inset of Fig. 3). We denote these two pairings as $\pm 2q_B$-FF pairings. Note that although these two pairings with opposite pairing momentum are nearly degenerate, the mixing of them is not favorable according to the GL free energy analysis up to the fourth order (see Supplemental Material, Sec. V [46]). Moreover, according to a phenomenological GL analysis in Sec. V, the interlayer coupling would increase the kinetic energy of the superconductor under in-plane magnetic fields due to the canonical momentum mixing between the two layers. On the other hand, the $2q_B$-FF pairing would lower this energy, which could make it more favorable than the zero-momentum pairing.

To obtain the $B - T$ phase diagram, we plot the critical B_{c2} (left axis, solid blue) and the corresponding stabilized $\boldsymbol{q} = (0, q)$ (right axis, red) as a function of temperature T in Fig. 3(c). The finite-momentum pairing ($q > 0$) is seen to emerge at temperature $T \approx 0.75T_c$, near where the B_c–T curve exhibits an upturn at the phase transition. Notably,

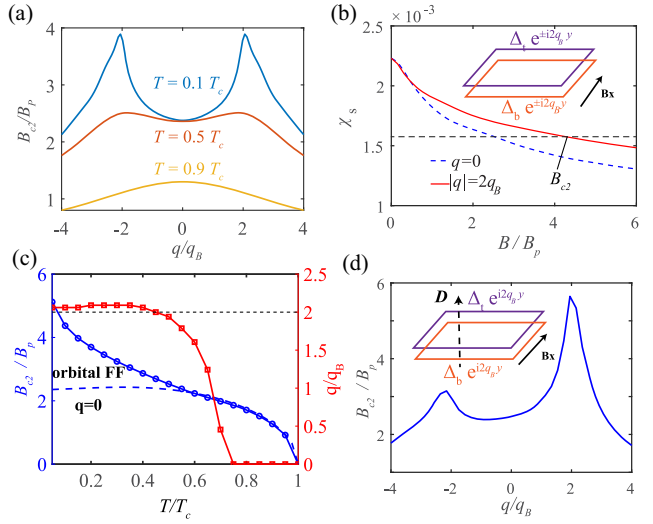

FIG. 3. (a) The in-plane B_{c2} versus pairing momentum q (in units of q_B) at various temperatures $T = 0.1T_c, 0.5T_c, 0.9T_c$. (b) The superconducting pairing susceptibility $\chi_s(q = 0)$ and $\chi_s(q = 2q_B)$ versus B, obtained from diagonalizing the pairing susceptibility matrix. The inset schematically plots the FF pairing with $q_y = 2q_B$ driven by an in-plane field B_x. (c) The left axis shows the B_{c2} versus T curve for finite-momentum q pairing (solid blue line) and zero-momentum pairing ($q = 0$), while the right axis (red line) shows the corresponding favorable pairing momentum q (in units of q_B) as a function of temperature. (d) The B_{c2} versus T curve upon a finite out-of-plane displacement field D. The inset schematically represents the $2q_B$-FF pairing under finite out-of-plane displacement fields D.

the momentum shifts q would saturate and the previously discussed $2q_B$-FF pairings emerge at low temperatures $T \lesssim 0.5T_c$. The finite-momentum pairing phase region, the boundary of which is roughly given by the B_c–T curve with $q = 0$ and finite q, is highlighted in Fig. 3(c). It can be seen that the $2q_B$-FF state can be stabilized with a temperature $T \lesssim 0.5T_c$ and a magnetic field B roughly higher than $2B_p$.

Finally, we point out that the degeneracy between $+2q_B$-FF pairing and $-2q_B$-FF pairing can be lifted extrinsically by out-of-plane displacement fields D, which induces layer asymmetry. As shown in Fig. 3(d), when an out-of-plane displacement field $D = 5$ meV is applied, the B_{c2} of $2q_B$ finite-momentum pairing becomes much higher than the B_{c2} of the $-2q_B$ pairing, implying that $+2q_B$-FF pairing would be the favorable finite-momentum pairing under a large in-plane magnetic field. Note that in the experiment, superconductivity of twisted bilayer TMDs occurs in the presence of a displacement field.

Gate-tunable superconducting diode effect.—Next, we demonstrate a gate-tunable superconducting diode effect based on the proposed $2q_B$-FF pairing in moiré Ising superconductors. The superconducting diode effect is characterized by the critical current difference between

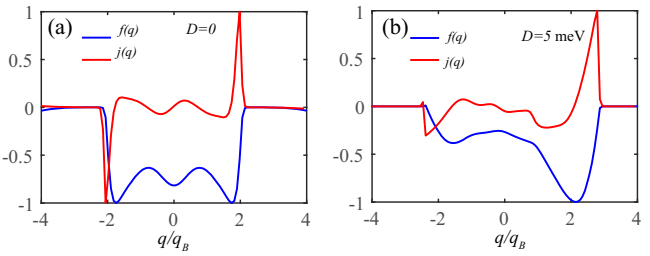

FIG. 4. (a) and (b) The free energy $f(q)$ and supercurrent $j(q)$ normalized to $[-1, 1]$ without displacement fields ($D = 0$ meV) and with a finite displacement field ($D = 5$ meV), respectively. Here the temperature $T = 0.1T_c$, and $B = 3B_p$ and $B = 2.5B_p$ for (a) and (b), respectively. In (a), the maximum magnitudes of $j(q)$ are the same in the positive and negative directions. This indicates the absence of the superconducting diode effect. In (b), the maximum magnitudes of $j(q)$ are different for currents flowing in opposite directions, indicating the presence of the superconducting diode effect.

currents flowing in opposite directions: $\Delta j_c = (j_{c,+} - |j_{c,-}|)/(j_{c,+} + |j_{c,-}|)$ [47–51], where the $+$ and $-$ signs denote the opposite current directions, respectively.

To demonstrate this, we can calculate the supercurrent $j(\boldsymbol{q})$ from the free energy [52]

$$f_s(\Delta, \boldsymbol{q}) = \frac{|\Delta|^2}{U_0} - \frac{1}{\beta}\sum_{\boldsymbol{k},n} \ln(1 + e^{-\beta\epsilon_{n\boldsymbol{q}}(\boldsymbol{k})}), \qquad (10)$$

where $\beta = 1/k_BT$, $\epsilon_{n\boldsymbol{q}}(\boldsymbol{k})$ is the quasiparticle energy of the finite-momentum Bogoliubov–de Gennes (BdG) Hamiltonian (see Supplemental Material, Sec. IV [46] for more details). The supercurrent $j(\boldsymbol{q})$ can be obtained by $j(\boldsymbol{q}) = 2[\partial f(\boldsymbol{q})]/\partial \boldsymbol{q}$, where $f(\boldsymbol{q})$ is the lowest free energy at each pairing momentum $\boldsymbol{q}$ and is given by minimizing the free energy $f_s(\Delta, \boldsymbol{q}) - f_n$ [note $f_n \equiv f_s(\Delta = 0)$ is the normal state free energy] with respect to Δ. Here, we consider the current direction to be along y direction so that we can denote $\boldsymbol{q} = (0, q)$.

The landscape of the minimized free energy $f(q)$ (blue line) and the corresponding supercurrent $j(q)$ (red line) in the case without displacement fields ($D = 0$) and with displacement fields ($D = 5$ meV) are plotted in Fig. 4. Here a large in-plane magnetic field [$B/B_p = 3$ and $B/B_p = 2.5$ for (a) and (b), respectively], and a temperature $T = 0.1T_c$ are adopted so that the system is deep in the FF pairing state. It is important to note that Ising SOC is very essential here. Without Ising SOC, the superconductivity could have been killed by the paramagnetic effect before reaching the FF state. Without displacement fields [Fig. 4(a)], the free energy of q near $\pm 2q_B$ is lower than $q = 0$ under a large B. In other words, $\pm 2q_B$-FF pairing would be stabilized, being consistent with the previous linearized gap equation calculation. However, the diode effect is absent ($\Delta j_c = 0$) in this case [Fig. 4(a)]. As shown

in Fig. 4(b), the diode effect becomes finite at finite displacement fields ($D = 5$ meV). Notably, the resulting $\Delta j_c \approx 53\%$ is much larger than the one proposed in superconductors with Rashba SOC [48]. This giant superconducting diode effect originates from the lifting of the degeneracy between $2q_B$-FF pairing and $-2q_B$-FF pairing by the displacement field, which enables a highly asymmetric free energy configuration as shown in Fig. 4(b). The implementation of an electric gate-tunable superconducting diode effect is generally difficult in previous systems [47,53,54], as the high electron density hinders the gate-controllability. The giant gate-tunable superconducting diode effect in the present system is potentially useful for dissipationless electronics, superconducting circuits and superconducting computing devices.

Discussion.—It is worth noting that the pairing form $\Delta(\boldsymbol{r})$ can be changed if the interlayer coupling strength can be tuned. For example, as shown in Supplemental Material, Sec. VI [46], we obtained a layer-antisymmetric FF pairing analytically, where $\Delta_t = |\Delta|e^{i\boldsymbol{q}\cdot\boldsymbol{r}}$ and $\Delta_b = |\Delta|e^{-i\boldsymbol{q}\cdot\boldsymbol{r}}$ with $\boldsymbol{q} = (0, 2q_B)$, in the case without twisting and in the weak interlayer coupling limit. We note that this exotic pairing has been proposed in centrosymmetric AB stacked bilayer TMDs without twisting previously [45]. This layer-antisymmetric FF pairing is energetically not favored in our case due to the stronger interlayer coupling strength, which increases the Josephson coupling energy. The orbital FF pairings we find would not afford such Josephson coupling energy and are particularly allowed by noncentrosymmetric superconductors.

In conclusion, we have proposed an intriguing noncentrosymmetric superconductor—moiré Ising superconductor, in which the Ising SOC is dominant over moiré bandwidth and can be readily realized in superconducting moiré TMDs. We have highlighted that moiré Ising superconductors are wonderful platforms for exploring novel superconducting effects, including orbital magnetic field-driven finite-momentum pairing state and gate-tunable superconducting diode effects. In principle, our theory for the orbital FF pairing state can also be applied to some other nontwisted superconducting materials with inversion broken and giant Ising SOC.

K. T. L. acknowledges the support of the Ministry of Science and Technology, China, and HKRGC through Grants No. 2020YFA0309600, No. RFS2021-6S03, No. C6025-19G, No. AoE/P-701/20, No. 16310520, No. 16310219, No. 16307622, and No. 16309718. Y. M. X. acknowledges the support of HKRGC through PDFS2223-6S01.

Note added.—Recently, we were informed by Ye that the orbital-field-driven finite-momentum pairing state might have been observed in multilayer 2H-$NbSe_2$ [55].

*ymxie@ust.hk
†phlaw@ust.hk

[1] Y. Cao, V. Fatemi, A. Demir, S. Fang, S. L. Tomarken, J. Y. Luo, J. D. Sanchez-Yamagishi, K. Watanabe, T. Taniguchi, E. Kaxiras, R. C. Ashoori, and P. Jarillo-Herrero, Nature (London) **556**, 80 (2018).
[2] Y. Cao, V. Fatemi, S. Fang, K. Watanabe, T. Taniguchi, E. Kaxiras, and P. Jarillo-Herrero, Nature (London) **556**, 43 (2018).
[3] E. Y. Andrei, D. K. Efetov, P. Jarillo-Herrero, A. H. MacDonald, K. F. Mak, T. Senthil, E. Tutuc, A. Yazdani, and A. F. Young, Nat. Rev. Mater. **6**, 201 (2021).
[4] F. Wu, T. Lovorn, E. Tutuc, and A. H. MacDonald, Phys. Rev. Lett. **121**, 026402 (2018).
[5] F. Wu, T. Lovorn, E. Tutuc, I. Martin, and A. H. MacDonald, Phys. Rev. Lett. **122**, 086402 (2019).
[6] L. Wang, E.-M. Shih, A. Ghiotto, L. Xian, D. A. Rhodes, C. Tan, M. Claassen, D. M. Kennes, Y. Bai, B. Kim, K. Watanabe, T. Taniguchi, X. Zhu, J. Hone, A. Rubio, A. N. Pasupathy, and C. R. Dean, Nat. Mater. **19**, 861 (2020).
[7] Z. Zhang, Y. Wang, K. Watanabe, T. Taniguchi, K. Ueno, E. Tutuc, and B. J. LeRoy, Nat. Phys. **16**, 1093 (2020).
[8] Y. Tang, L. Li, T. Li, Y. Xu, S. Liu, K. Barmak, K. Watanabe, T. Taniguchi, A. H. MacDonald, J. Shan, and K. F. Mak, Nature (London) **579**, 353 (2020).
[9] E. C. Regan, D. Wang, C. Jin, M. I. Bakti Utama, B. Gao, X. Wei, S. Zhao, W. Zhao, Z. Zhang, K. Yumigeta, M. Blei, J. D. Carlström, K. Watanabe, T. Taniguchi, S. Tongay, M. Crommie, A. Zettl, and F. Wang, Nature (London) **579**, 359 (2020).
[10] Y. Xu, S. Liu, D. A. Rhodes, K. Watanabe, T. Taniguchi, J. Hone, V. Elser, K. F. Mak, and J. Shan, Nature (London) **587**, 214 (2020).
[11] X. Huang, T. Wang, S. Miao, C. Wang, Z. Li, Z. Lian, T. Taniguchi, K. Watanabe, S. Okamoto, D. Xiao, S.-F. Shi, and Y.-T. Cui, Nat. Phys. **17**, 715 (2021).
[12] Y. Zhang, N. F. Q. Yuan, and L. Fu, Phys. Rev. B **102**, 201115(R) (2020).
[13] C. Jin, Z. Tao, T. Li, Y. Xu, Y. Tang, J. Zhu, S. Liu, K. Watanabe, T. Taniguchi, J. C. Hone, L. Fu, J. Shan, and K. F. Mak, Nat. Mater. **20**, 940 (2021).
[14] T. Li, S. Jiang, B. Shen, Y. Zhang, L. Li, Z. Tao, T. Devakul, K. Watanabe, T. Taniguchi, L. Fu, J. Shan, and K. F. Mak, Nature (London) **600**, 641 (2021).
[15] K. F. Mak and J. Shan, Nat. Nanotechnol. **17**, 686 (2022).
[16] L. An, X. Cai, D. Pei, M. Huang, Z. Wu, Z. Zhou, J. Lin, Z. Ying, Z. Ye, X. Feng *et al.*, Nanoscale Horizons **5**, 1309 (2020).
[17] Y.-T. Hsu, F. Wu, and S. Das Sarma, Phys. Rev. B **104**, 195134 (2021).
[18] C. Schrade and L. Fu, arXiv:2110.10172.
[19] L. Klebl, A. Fischer, L. Classen, M. M. Scherer, and D. M. Kennes, Phys. Rev. Res. **5**, L012034 (2023).
[20] Y.-M. Wu, Z. Wu, and H. Yao, Phys. Rev. Lett. **130**, 126001 (2023).
[21] A. Wietek, J. Wang, J. Zang, J. Cano, A. Georges, and A. Millis, Phys. Rev. Res. **4**, 043048 (2022).
[22] B. Zhou and Y.-H. Zhang, arXiv:2209.10023.

[23] M. Bélanger, J. Fournier, and D. Sénéchal, Phys. Rev. B **106**, 235135 (2022).
[24] G.-B. Liu, W.-Y. Shan, Y. Yao, W. Yao, and D. Xiao, Phys. Rev. B **88**, 085433 (2013).
[25] D. Xiao, G.-B. Liu, W. Feng, X. Xu, and W. Yao, Phys. Rev. Lett. **108**, 196802 (2012).
[26] J. M. Lu, O. Zheliuk, I. Leermakers, N. F. Q. Yuan, U. Zeitler, K. T. Law, and J. T. Ye, Science **350**, 1353 (2015).
[27] X. Xi, Z. Wang, W. Zhao, J.-H. Park, K. T. Law, H. Berger, L. Forró, J. Shan, and K. F. Mak, Nat. Phys. **12**, 139 (2016).
[28] Y. Saito, Y. Nakamura, M. S. Bahramy, Y. Kohama, J. Ye, Y. Kasahara, Y. Nakagawa, M. Onga, M. Tokunaga, T. Nojima, Y. Yanase, and Y. Iwasa, Nat. Phys. **12**, 144 (2016).
[29] S. C. de la Barrera, M. R. Sinko, D. P. Gopalan, N. Sivadas, K. L. Seyler, K. Watanabe, T. Taniguchi, A. W. Tsen, X. Xu, D. Xiao, and B. M. Hunt, Nat. Commun. **9**, 1427 (2018).
[30] J. Lu, O. Zheliuk, Q. Chen, I. Leermakers, N. E. Hussey, U. Zeitler, and J. Ye, Proc. Natl. Acad. Sci. U.S.A. **115**, 3551 (2018).
[31] Y. Xing, K. Zhao, P. Shan, F. Zheng, Y. Zhang, H. Fu, Y. Liu, M. Tian, C. Xi, H. Liu, J. Feng, X. Lin, S. Ji, X. Chen, Q.-K. Xue, and J. Wang, Nano Lett. **17**, 6802 (2017).
[32] E. Sohn, X. Xi, W.-Y. He, S. Jiang, Z. Wang, K. Kang, J.-H. Park, H. Berger, L. Forró, K. T. Law, J. Shan, and K. F. Mak, Nat. Mater. **17**, 504 (2018).
[33] B. T. Zhou, N. F. Q. Yuan, H.-L. Jiang, and K. T. Law, Phys. Rev. B **93**, 180501(R) (2016).
[34] W.-Y. He, B. T. Zhou, J. J. He, N. F. Q. Yuan, T. Zhang, and K. T. Law, Commun. Phys. **1**, 40 (2018).
[35] Y. Xie, B. T. Zhou, T. K. Ng, and K. T. Law, Phys. Rev. Res. **2**, 013026 (2020).
[36] G. Sharma and S. Tewari, Phys. Rev. B **94**, 094515 (2016).
[37] S. Ilić, J. S. Meyer, and M. Houzet, Phys. Rev. Lett. **119**, 117001 (2017).
[38] J. Zhang and V. Aji, Phys. Rev. B **94**, 060501(R) (2016).
[39] Y. Nakamura and Y. Yanase, Phys. Rev. B **96**, 054501 (2017).
[40] Y.-T. Hsu, A. Vaezi, M. H. Fischer, and E.-A. Kim, Nat. Commun. **8**, 14985 (2017).
[41] D. Wickramaratne, S. Khmelevskyi, D. F. Agterberg, and I. I. Mazin, Phys. Rev. X **10**, 041003 (2020).
[42] A. M. Clogston, Phys. Rev. Lett. **9**, 266 (1962).
[43] B. S. Chandrasekhar, Appl. Phys. Lett. **1**, 7 (1962).
[44] P. Fulde and R. A. Ferrell, Phys. Rev. **135**, A550 (1964).
[45] C.-X. Liu, Phys. Rev. Lett. **118**, 087001 (2017).
[46] See Supplemental Material at http://link.aps.org/supplemental/10.1103/PhysRevLett.131.016001 for (i) details for the moiré potential and model parameters; (ii) pairing classifications for twisted bilayer TMD; (iii) extended figures; (iv) the linearized gap equation and free energy for the finite momentum pairing; (v) Ginzburg-Landau Free energy for a bilayer superconductor under in-plane orbital magnetic fields; (vi) the layer anti-symmetric $2q_B$ FF pairing in AA stacking bilayer TMD in the weak interlayer coupling limit.
[47] F. Ando, Y. Miyasaka, T. Li, J. Ishizuka, T. Arakawa, Y. Shiota, T. Moriyama, Y. Yanase, and T. Ono, Nature (London) **584**, 373 (2020).
[48] A. Daido, Y. Ikeda, and Y. Yanase, Phys. Rev. Lett. **128**, 037001 (2022).
[49] N. F. Q. Yuan and L. Fu, Proc. Natl. Acad. Sci. U.S.A. **119**, e2119548119 (2022).
[50] J. J. He, Y. Tanaka, and N. Nagaosa, New J. Phys. **24**, 053014 (2022).
[51] S. Ilić and F. S. Bergeret, Phys. Rev. Lett. **128**, 177001 (2022).
[52] Y.-M. Xie, B. T. Zhou, and K. T. Law, Phys. Rev. Lett. **125**, 107001 (2020).
[53] H. Wu, Y. Wang, Y. Xu, P. K. Sivakumar, C. Pasco, U. Filippozzi, S. S. P. Parkin, Y.-J. Zeng, T. McQueen, and M. N. Ali, Nature (London) **604**, 653 (2022).
[54] L. Bauriedl, C. Bäuml, L. Fuchs, C. Baumgartner, N. Paulik, J. M. Bauer, K.-Q. Lin, J. M. Lupton, T. Taniguchi, K. Watanabe, C. Strunk, and N. Paradiso, Nat. Commun. **13**, 4266 (2022).
[55] P. Wan, O. Zheliuk, N. F. Q. Yuan, X. Peng, L. Zhang, M. Liang, U. Zeitler, S. Wiedmann, N. E. Hussey, T. T. M. Palstra, and J. Ye, Nature (London) (2023).